



The Fourier transform infrared spectroscopy (FTIR) analysis for the clay mineralogy studies in a clastic reservoir

Golnaz Jozanikohan¹ · Mohsen Nosrati Abarghoeei²

Received: 17 August 2021 / Accepted: 27 December 2021 / Published online: 9 January 2022
© The Author(s) 2022

Abstract

The complete characteristics knowledge of clay minerals is necessary in the evaluation studies of hydrocarbon reservoirs. Ten samples taken from two wells in a heterogeneous clastic gas reservoir formation in NE Iran were selected to conduct the transmission Fourier transform infrared spectroscopy (FTIR) tests for the clay mineralogy studies. The FTIR analysis showed that there were clear signs of clay minerals in all samples. The wavenumber region of the clay minerals in FTIR tests was detected to be 3621, 3432, 1034, and 515 cm^{-1} for illite, 3567, 3432, 1613, 1088, 990, 687, 651, and 515 cm^{-1} for magnesium-rich chlorite, 3700, 3621, 3432, 1034, 687, and 463 cm^{-1} for kaolinite, and 3567, 1088, 990, and 463 cm^{-1} for glauconite. After screening of samples by the FTIR method, the samples were then analyzed by powder X-ray diffraction (PXRD), wavelength dispersive X-ray fluorescence (WDXRF), and scanning electron microscopy (SEM). The PXRD and SEM result showed illite was by far the most common clay present. Kaolinite, magnesium-rich chlorite, and traces of smectite and the mixed-layer clays of both the illite–smectite and chlorite–smectite types were also recognized. The combination of PXRD and WDXRF results could quantify the clay abundances in the each well too. It was concluded that the FTIR analysis successfully could show the absorption bonds of all constituent clays. However, the infrared absorption spectra of mixed-layer clays overlapped those of the respective constituents of each mixed-layer minerals. This can be considered as the evidence of the usefulness of FTIR technique in the screening of the samples for the clay mineralogy studies.

Keywords Transmission Fourier transform infrared spectroscopy (FTIR) · Powder X-ray diffraction (PXRD) · Wavelength dispersive X-ray fluorescence (WDXRF) · The clay minerals

Introduction

The clay minerals, even in the small amounts, strongly affect the properties of petroleum reservoirs as well as the response of most well logging tools (Attia et al. 2015; Abudeif et al. 2016a, 2016b, 2018; Hasan et al. 2020; Radwan 2020; Radwan et al. 2020; Jiu et al. 2021). Thus, a comprehensive knowledge of clay mineralogy is needed for both the reservoir modeling and the interpretation of wire-line log data (Hong et al. 2020; Wang et al. 2020; Radwan, 2021a;

Radwan et al., 2021a). In addition, clays may react with drilling fluids causing formation damage (Radwan et al. 2019a; Radwan et al. 2019b; Radwan 2020, 2021b; Radwan et al. 2021b, 2021c), so a good knowledge of clay mineralogy may influence the choice of drilling fluids and additives. Number of techniques has been used to characterize the individual clay minerals (Ashraf et al. 2019; Ali et al. 2020) of which the X-ray diffraction (XRD) is the most popular one (Jozanikohan et al. 2016; Abd Elmola et al. 2020). The conventional XRD method needs careful sample preparation besides several specialized treatments to identify particular clay minerals (Kumar & Lingfa 2020). However, such treatments run the risk of destroying or altering clays of interest (Moore & Reynolds 1989). Infrared spectroscopy (IR) is a widely used analytical technique in the geosciences studies (Stanienda 2016) and sometimes used as a screening tool to recognize the samples containing clays for more sophisticated and time-consuming procedures such as XRD. The FTIR analysis has several advantages over the XRD including: (i) the

✉ Golnaz Jozanikohan
gjkohan@ut.ac.ir

Mohsen Nosrati Abarghoeei
nosrati21503@gmail.com

¹ School of Mining, College of Engineering, University of Tehran, 14399-57131 Tehran, Iran

² Department of Mining and Metallurgical Engineering, Yazd University, 8915818411 Yazd, Iran

preparation of powder samples is quite easy and fast (KBr pellets normally take 5–8 min to be ready); (ii) the collection of spectrum is fast (it takes almost 1–2 min), (iii) only small amount of samples (about 0.3 g) are required; (iv) additional treatments of samples are not required, and (v) it is cheap compared to the XRD method (Madejová & Komadel 2001; Ji et al. 2009; Pálková et al. 2020). The spectral absorption characteristics in the IR spectra are qualitatively related to the variations in the constituent minerals and can be used for investigating the crystalline structure, type of bonding, and some chemical information on the clay minerals (Madejová, 2003; Du et al. 2010; Yan et al. 2021). The Fourier transforms of IR spectra are being increasingly used to aid the clay mineral identification (Madejová, 2003; Vaculíková & Plevová, 2005; Nayak & Singh 2007; Worasith et al. 2011; Repacholi 1994; Djomgoue & Njopwouo 2013; Chen et al. 2020; El-Shater et al. 2021). The high signal-to-noise ratios as well as the high speed of data acquisition and accuracy enhancement in frequency measurements have made the FTIR method a suitable candidate for the initial analysis method to characterize the clay minerals (Madejová, 2003; Ma et al. 2021).

The clay minerals consist of hydroxyl groups, tetrahedral and octahedral sheets, and interlayer cations (Meunier 2005). The valuable “fingerprint” absorptions in clay mineral characterization are mainly contributed by the stretching and bending vibration bands of Si–O, Al–O, and O–H (Farmer 2000). The absorption of IR radiation by individual clay minerals are determined by the strength, length, and force constants of chemical bonds in the structures of clay minerals as well as crystalline order, shape and size of particles, atomic mass, and some symmetry-related elements such as the unit cell constraints of the symmetry, and finally the local site symmetry of each individual atom within the unit cell (Repacholi 1994). Different aspects of clay mineralogy, including the study of relationships between the clay chemical composition and the absorption band variations, and the study of variations in the absorption features after acid treatment/heating were carried out using the FTIR analysis (Madejová et al. 1998; Tyagi et al. 2006). In nature, clay minerals are often accompanied by quartz, K-feldspar and plagioclase, carbonates, iron oxide, and/or sulfide or sulfates (Meunier 2005). Differences in the absorption bands of these non-clay minerals make them clearly distinguishable from each other. The clay minerals can exclusively be differentiated from the other minerals by the absorption bands of structural OH and Si–O groups. However, each clay mineral may have similar types of bonds, which make them more difficult to distinguish (Farmer 2000).

The contribution of the FTIR method in the oil and gas industry has been included, but not limited to the determinations of oil acidity (Li 2009), the assessment of the shale gas and shale oil potentials (Wright et al. 2015), the study

of the petroleum fluid inclusions (Li & Parnell 2003), the assessment of the pyrolysis gases (Pimpke et al. 2020), the identification of the insoluble fraction of pyrolysis oil (Scholze & Meier 2001), the composition characterization of the collected bio-oils (Shen et al. 2010), the study of the chemical structures of individual macerals as well as their relative generation kinetics (Lin & Ritz 1993).

Some previous FTIR studies on the pure clay minerals have been carried out (Madejová, 2003; Nayak & Singh 2007; Repacholi 1994; Du et al. 2010), but analogously little consideration has been given to the identification of the clay minerals in the clastic formations with complex lithologies by the transmission FTIR method (Adamu 2010). Since the Shurijeh formation is considered as a heterogeneous sandstone reservoirs, it needs to be mineralogically identified in the eastern part of Kopet-Dagh sedimentary Basin, NE Iran. In this research, the ability of one of the most famous spectral analysis methods, i.e., transmission Fourier transform infrared (FTIR) spectroscopy, as a screening tool, has been investigated to select the samples containing clays, for further studies along with the traditional methods such as powder X-ray diffraction (PXRD), wavelength dispersive X-ray fluorescence (WDXRF), and the scanning electron microscopy (SEM) analysis. The results of this study will aid the geoscientists in oil and gas upstream industries to evaluate and screen the samples for the purpose of clay mineralogy studies in reservoir evaluation stages more fast and convenient, before conducting expensive and time-consuming analysis such as the XRD, SEM, and XRF.

Experimental methods

Materials

The coring operation was conducted on the reservoir formation at depths of 3202.8–3210 m and 3180–3207.6 m of the gas-producing and non-producing wells, respectively. A total of 76 core samples was taken almost every one and a half meter from the Shurijeh formation in a gas-producing well and a non-producing one. The wells are located in the Iranian part of eastern Kopet-Dagh Basin, NE Iran (Fig. 1). The understudy reservoir formation is mainly composed of sandstone with interlayer of clay minerals. Therefore, all of the collected core samples did not contain the clay minerals in the major quantities. Ten samples were carefully selected based on the macroscopic features related to the lithological variations such as texture, grain size, cementation, beddings, and looseness degree to determine the samples containing the most amounts of clay minerals for further detailed analysis methods. Five samples, labeled with “GP,” were taken from the gas-producing well between the depths of

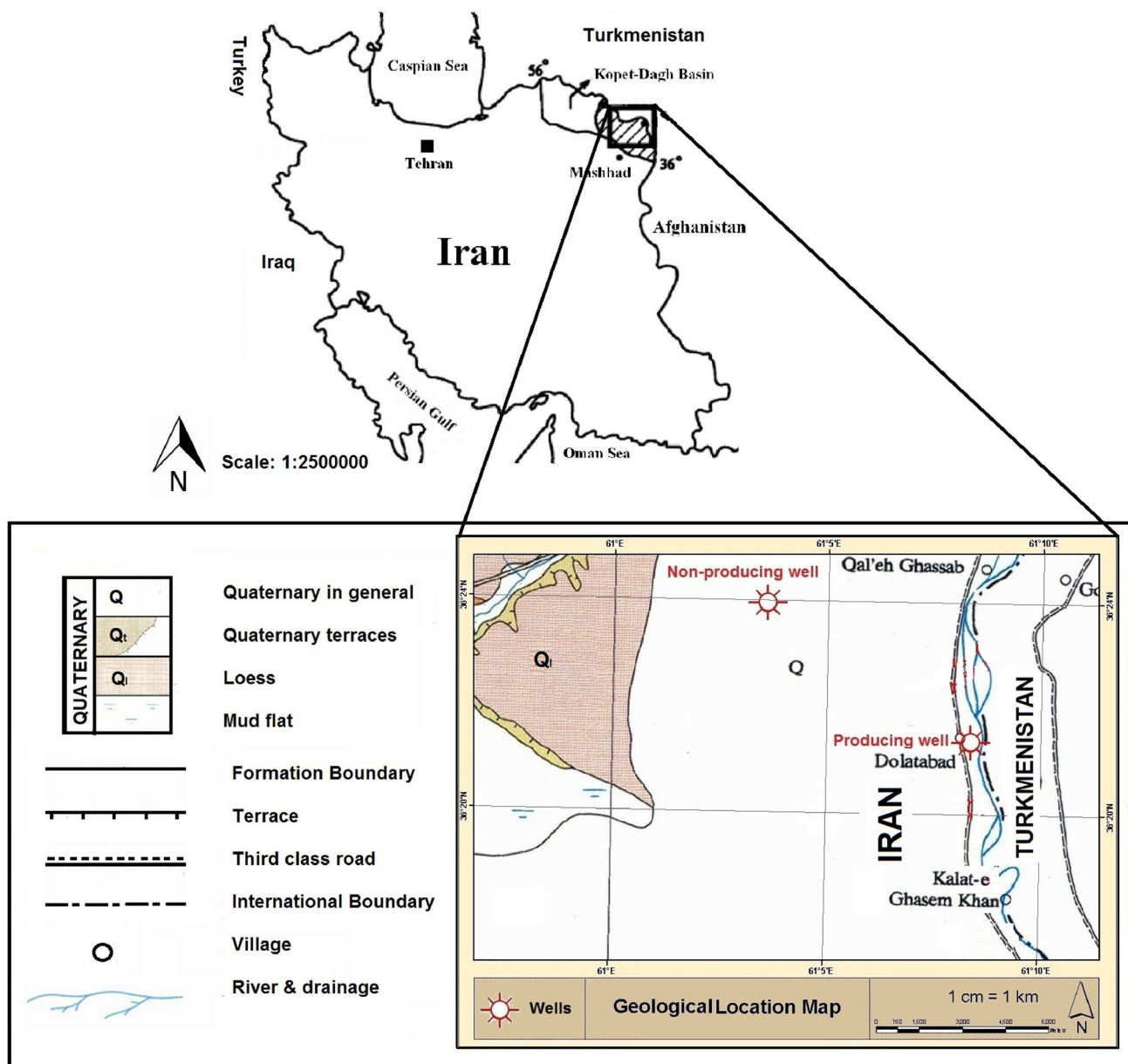


Fig. 1 Geographic location map of the studied area, modified from Jozanikohan et al. 2015

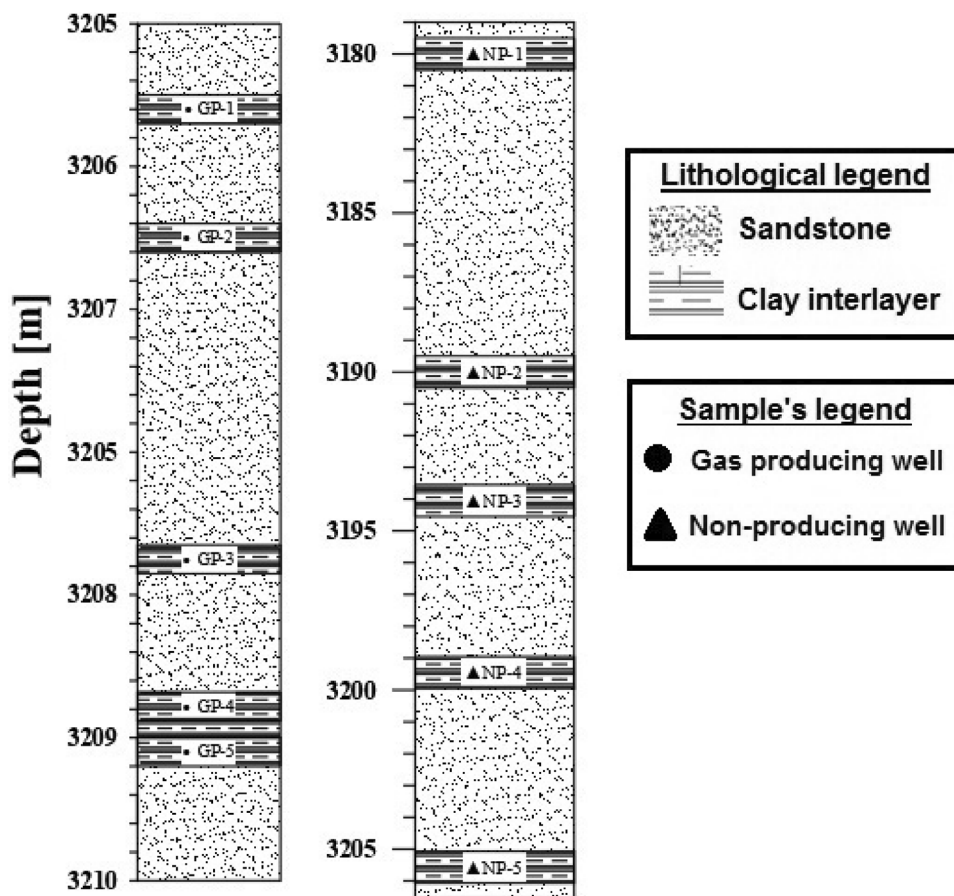
3204.6 and 3209.1 m, and the remaining samples, labeled with “NP,” were selected from depths of 3180–3205.57 m in the non-producing well. The outside parts of each core sample were carefully removed to avoid from the possible contaminations or oxidation effects. The samples were then ground to pass through a 200- μ m sieve and carefully mixed to give a homogeneous mixture. The location of each sample is shown in Fig. 2. All of the ten samples were made ready to be analyzed by the FTIR method.

Methods

Transmission Fourier transform infrared (FTIR) spectroscopy

The vibrational spectra for all samples were obtained using a Bruker TENSOR 27 FTIR spectrometer, equipped with an infrared source, potassium bromide beam splitter, and high sensitive DigiTect™ detector system. Disks of 13-mm diameter and 1–2-mm thickness, consisting of

Fig. 2 Schematic core sample locations of the both wells. Sample codes and the lithological units are shown. Right: Gas-producing well, and Left: Non-producing well



approximately 0.6 mg sample gently dispersed in 200 mg of KBr, were carefully heated at 120 °C to minimize the amount of the absorbed water. Disks were then immediately and thoroughly scanned in the wavenumber region of 4000–400 cm^{-1} in transmission mode with a resolution of 4 cm^{-1} with 128 successive scans.

Powder X-ray diffraction (PXRD) analysis

The most important step in the quantitative XRD analysis is to prepare the samples with respect to all the possible sources of error. To gain a preliminary knowledge of the existing minerals, the randomly oriented powder samples were first exposed to the X-ray and analyzed. A Bruker AXS, D8 Advance X-ray powder diffractometer with $\text{CuK}\alpha$ radiation and a 2theta/theta goniometer was used for the XRD analysis. Diffraction patterns of the samples were recorded by the step scanning from 4 to 70 degrees (2θ), with a step size of 0.02° and counting for 5 s per step at 40 kV and 30 mA.

Since the non-clays can cover up some basic reflections of the clay minerals, thus the non-clay separation is a necessary task which was performed based on the procedure described by Moore & Reynolds (1989). The chemical

procedure for removal of XRD-proved non-clays, i.e., carbonate and sulfate minerals was to use the mild heating of the samples in a $\text{C}_2\text{H}_3\text{NaO}_2\text{--CH}_3\text{COOH}$ buffer at pH = 5 (Jackson and Barak 2005), and also with using the sodium salt of $\text{C}_{10}\text{H}_{16}\text{N}_2\text{O}_8$ (EDTA) (Bodine and Fernald 1973), respectively. The iron oxide content of samples was negligible, and to avoid the risk of peak alteration in the mixed-layer clay minerals and or dissolution of iron-rich chlorite minerals, the iron content was not removed. The physical procedure for removal of other minerals such as quartz, plagioclase, and alkali feldspars was to settle them in a coarser residue of a wide-mouth glass tube, on the basis of Stokes' law. After several times of decantation the supernate, the clay fraction (< 2 μm) was extracted after 246 min at 20 °C. To prevent the clays from forming the polymineralic aggregates, a 0.1% solution of sodium hexametaphosphate was used in the each removal stage to disperse the clay minerals into the individual colloidal particles. Four small homogeneous glass slides were prepared from smearing the paste of < 2 μm . The XRD analyses were then performed from 4 to 40 (2θ) degrees on four oriented clay small glass slides of naturally dried in the air, saturated with the $\text{C}_2\text{H}_6\text{O}_2$ (ethylene glycol) vapor, boiled in the hydrochloric acid, and heated.

Wavelength dispersive X-ray fluorescence (WDXRF)

Elemental analysis of the Shurijeh samples was performed on an automated Philips MagiX PRO wavelength dispersive X-ray fluorescence (WDXRF) spectrometer. Loss on ignition (LOI) was also determined (Table 1).

The mineral quantification based on a combined analysis method (XRD-XRF)

Several distinguished researches have proved that the mineral quantification could be done by means of combination of chemical and mineralogical data obtained from the XRF and XRD test, respectively (Paktunc 2001; Prandel et al. 2014; Jozanikohan et al. 2016; Zhang et al. 2020, 2021). Method basically includes solving a series of formulated simultaneous equations relating the chemical composition data to the percentages of each individual mineral (Eq. 1 to i).

$$\alpha_{_1} A + b_{_1} \beta + \dots + \omega_{_1} Z = 100k_{_1} \quad (1)$$

$$\alpha_{_2} A + b_{_2} \beta + \dots + \omega_{_2} Z = 100k_{_2} \quad (2)$$

$$\begin{aligned} \alpha_{_3} A + b_{_3} \beta + \dots + \omega_{_3} Z &= 100k_{_3} \\ &\vdots \\ \alpha_{_i} A + b_{_i} \beta + \dots + \omega_{_i} Z &= 100k_{_i} \end{aligned} \quad (3)$$

where $\alpha_{_i}$, $\beta_{_i}$, ..., $\omega_{_i}$, and $k_{_i}$, display the *i*th element percentages in the each individual mineral phases and the whole bulk rock, respectively. A, B, ..., and Z indicate the present phases percentages in the studied sample.

In the current study, the combined XRD–XRF method has been used for the phase quantification purpose. Having identified the main constituents of the samples and the relevant chemical formula from the PXRD analysis, a quantification method based on what explained above were applied, using the elemental analyses provided from the XRF data to estimate the mineral abundances.

The average percentages of each individual phase and each of the clay minerals are given in Tables 2 and 3, respectively.

Table 1 XRF results of the Shurijeh core samples

Code	MgO (%)	Al ₂ O ₃ (%)	SiO ₂ (%)	SO ₃ (%)	K ₂ O (%)	CaO (%)	Fe ₂ O ₃ (%)	Na ₂ O (%)	LOI (%)	Total (%)
GP-1	1.20	11.28	74.21	0.65	2.50	3.76	0.72	3.26	2.42	100
GP-2	0.59	8.20	68.59	7.70	2.00	8.19	1.23	1.47	2.03	100
GP-3	1.99	12.24	64.84	4.29	3.53	5.47	3.14	1.38	3.12	100
GP-4	4.43	9.51	65.26	0.00	2.92	5.71	2.99	0.82	8.36	100
GP-5	1.68	5.92	69.20	6.00	2.04	8.04	0.71	1.20	5.21	100
NP-1	3.41	10.24	66.14	1.18	2.33	5.93	1.35	2.66	6.76	100
NP-2	1.60	13.41	66.16	1.71	3.27	5.70	3.08	1.59	3.48	100
NP-3	2.61	11.34	57.59	6.29	3.04	9.09	2.17	1.24	6.63	100
NP-4	3.90	13.06	53.22	4.35	3.00	9.79	2.61	1.60	8.47	100
NP-5	3.61	12.80	50.83	7.00	2.92	10.05	4.42	1.09	7.28	100

Table 2 Mineral content of the Shurijeh core samples

Code	Quartz (%)	Plagioclase (%)	K-feldspar (%)	Anhydrite (%)	Carbonate (%)	Hematite (%)	Clays (%)	Total (%)
GP-1	65.5	17.1	4.6	1.1	4.0	0.0	7.7	100
GP-2	61.5	12.1	4.0	13.1	3.0	0.0	6.3	100
GP-3	53.0	12.5	6.1	7.3	3.7	0.8	16.6	100
GP-4	56.1	9.7	4.1	0.0	15.3	1.1	13.7	100
GP-5	64.4	6.6	3.0	10.2	8.3	0.0	7.5	100
NP-1	47.7	24.5	6.0	2.0	13.0	0.0	6.8	100
NP-2	54.7	15.7	4.9	2.9	5.5	1.1	15.2	100
NP-3	46.2	12.6	3.7	10.7	11.2	1.1	14.5	100
NP-4	39.9	18.2	3.2	7.4	15.4	1.5	14.4	100
NP-5	39.3	13.2	2.0	11.9	11.9	2.9	18.8	100

Table 3 Clay contents of the Shurijeh core samples, obtained from the XRD test

Code	Kaolinite (%)	Chlorite (%)	Illite (%)	Glaucanite (%)	Smectite (%)	Mixed-layer Clays (%)	Total (%)
GP-1	1.6	1.3	2.8	2.0	0.0	0.0	7.7
GP-2	1.1	1.8	1.7	1.7	0.0	0.0	6.3
GP-3	4.7	5.7	6.2	0.0	0.0	0.0	16.6
GP-4	1.8	4.6	6.5	0.0	0.8	0.0	13.7
GP-5	1.0	1.1	2.7	2.7	0.0	0.0	7.5
NP-1	2.0	3.0	0.5	1.3	0.0	0.0	6.8
NP-2	2.5	3.4	3.1	6.2	0.0	0.0	15.2
NP-3	2.4	2.6	6.0	0.0	0.0	3.5	14.5
NP-4	2.4	2.7	8.1	0.0	0.0	1.2	14.4
NP-5	4.1	3.7	9.5	0.0	0.0	1.5	18.8

The scanning electron microscopy (SEM) analysis

The scanning electron microscopy technique (SEM) was engaged to characterize the morphology, geometry, and distribution patterns of clay minerals in some of the selected samples. The selection procedure was accomplished based on the clay content of each sample determined by the XRD method. The selected samples (i.e., GP-3, GP-4, NP-2, and NP-3) were fully coated with thin layers of gold–palladium for 60 s. The SEM analyses were then conducted using a JEOL model JSM-840.

The results

The data in Table 1 show the chemical composition of ten mentioned core samples in both wells, obtained from the XRF test.

According to the whole-rock powder diffractometry, the main constituents of the samples from both wells are quartz, and plagioclase with the secondary minerals such as clays, anhydrite, carbonates (dolomite and calcite), and K-feldspar (Fig. 3a). Hematite was observed in some few samples. These XRD results were found extremely useful in the designing of the subsequent non-clay mineral removal steps (Fig. 3b). The identified clay minerals were kaolinite, illite, glauconite, chlorite, smectite, and mixed layers of illite–smectite, and chlorite–smectite types.

The obtained SEM images are shown in Fig. 4. It is clear from Fig. 4 that the most common pore filling clay minerals included kaolinite with platy morphology and illite as microfibrils. In all of the studied samples, kaolinite were mainly found as several stacking of successive layers (e.g., Fig. 4a), and fully filled the pores. The fine illite fibers (Fig. 4b) were widely spread in the open pore space, changing the macro-porosities to micro-porosities. The assemblages of mixed-layer clays such as illite–smectite

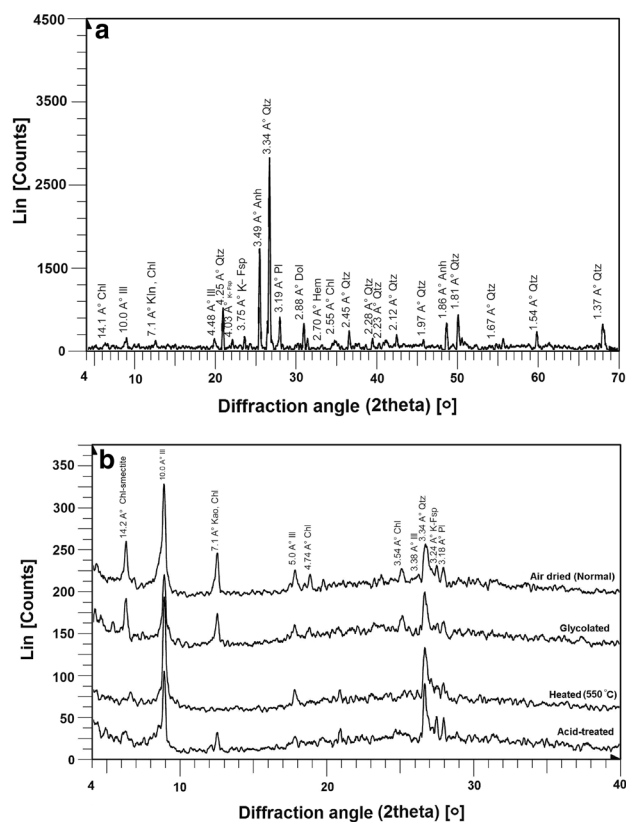


Fig. 3 **a** Whole-rock powder X-ray diffraction pattern of the samples under study (Sample code: NP-5); **b** The XRD diffraction pattern of the same sample. Chl=Chlorite, Chl–Smectite=Chlorite–smectite, Ill=Illite, Kao=Kaolinite, Qtz=Quartz, Pl=Plagioclase, Hem=Hematite, Anh=Anhydrite, Dol=Dolomite

are shown in Fig. 4c. Figure 4d shows chlorite intercalated with kaolinite found as grain coatings. The restricted pore geometry characterized by the SEM test showed very fine confined polygons with maximum 1.5 micro-meter diameter.

Fig. 4 SEM images of the samples under study: **a** GP-3 at 7000X magnification, 15 kV, and WD=23 mm; **b** GP-4 at 25500X magnification, 30 kV, and WD=23 mm; **c** NP-2 at 4000X magnification, 15 kV, and WD=24 mm; and **d** NP-3 at 2500X magnification, 15 kV, and WD=24 mm. Kao: kaolinite, Ill: Illite, Ill/Sm: Illite–smectite, Chl: chlorite

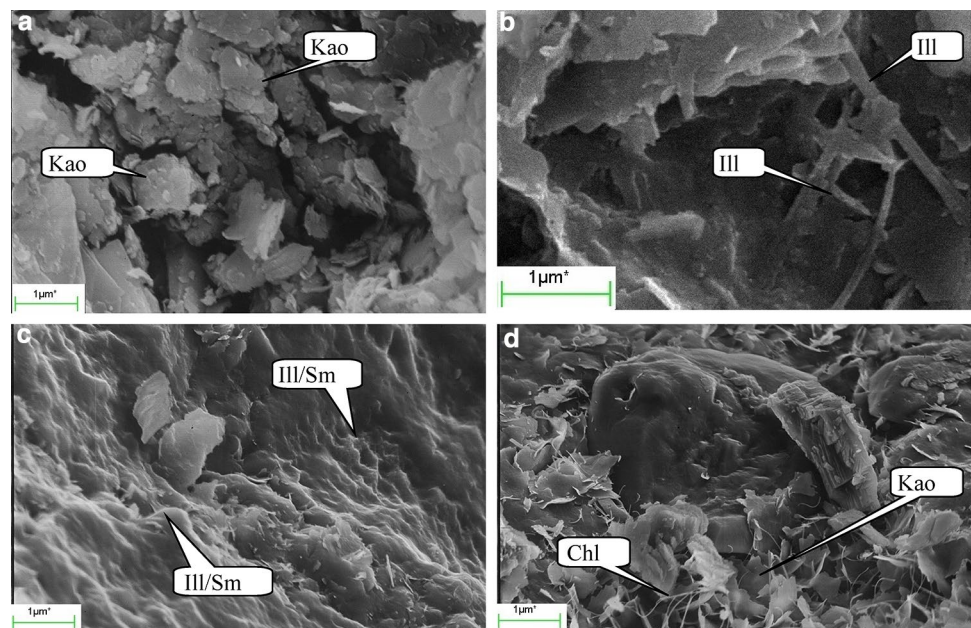


Figure 5 shows the infrared absorption spectra of the Shurijeh core samples. The splitting bands in the region of 800–400 cm^{-1} including 780, 693, 588, 533, 464, and 428 cm^{-1} as well as one band at 1034 cm^{-1} indicate the feldspar presence (Farmer 2000). According to the reports of some researches (Ji et al. 2009), the IR transmission spectra of carbonates include some distinctive features at 3050–2850 cm^{-1} , 2650–2500 cm^{-1} , 1790–1820 cm^{-1} , 1400–1500 cm^{-1} , 877 cm^{-1} , 730 cm^{-1} , and 710 cm^{-1} . However, the peak at 877 cm^{-1} was only observed in the Shurijeh samples containing more than 10% carbonate (e.g., GP-4, NP-1, NP-3, NP-4, and NP-5). Dolomite, in comparison with calcite, shows three characteristic absorptions at 3020, 2626, and 730 cm^{-1} (Ji et al. 2009). Since these FTIR bands are all present in the samples whose codes were mentioned above, the dolomite was identified as one of the components of the samples. The sulfates are demonstrated to have strong absorption bands near 980 cm^{-1} , 450 cm^{-1} , 1150–1100 cm^{-1} , and 675–590 cm^{-1} for SO_4 different vibrations (Uusitalo et al. 2020). The vibrations observed at 650 cm^{-1} , 525 cm^{-1} , 440–400 cm^{-1} , and 300 cm^{-1} indicate the possible presence of hematite (Ji et al. 2009). It is commonly believed that the Si–O stretching vibrations are observed at 800–1200 cm^{-1} , and its relative bending bands are found in the 400–600 cm^{-1} in the FTIR spectra of minerals (Matteson & Herron 1993).

Although the samples were heated and dried before the analysis, the clear band in the area 1640–1600 cm^{-1} could be assigned to the deformation vibrations of OH-adsorbed water (Kuligiewicz & Derkowski 2017) or it can be related to the magnesium-rich chlorite. The strong bands between 3400 and 3750 cm^{-1} were assigned to the hydroxyl linkage (O–H) (Balan et al. 2001). However, the broad characteristic bands

at 3450 and 3622 cm^{-1} suggest the possibility of hydration or layer hydrogen bonding in the samples (Kasprzhitskii et al. 2018). The well-resolved bands at 1120–1000 cm^{-1} region belong to the Si–O stretching vibration of kaolinite (Madejová & Komadel 2001). Kaolinite (1:1 layer) always shows a narrow, weak absorption at 3620 cm^{-1} due to the inner OH hydroxyls. Other hydroxyls give bands at higher cm^{-1} , while illite (2:1 layer) and smectite show wide absorption in the region of 3650–2600 cm^{-1} with a shoulder peak (Balan et al. 2001). Most of the relatively strong O–H vibration in smectite is from the water in the interlayer space of the silica tetrahedral sheet, which results in a wide absorption in the region of 3650–2600 cm^{-1} followed by the stronger absorption in about 1600 cm^{-1} (Changwen et al. 2007). The corresponding values for each vibration bands are given in Table 4.

The observed bands for each Shurijeh core sample in the range of 4000–400 cm^{-1} have been tentatively assigned (Fig. 5 and Table 5). The presences of bands at about 1086 cm^{-1} , 798 cm^{-1} , 778 cm^{-1} , 695 cm^{-1} , and 468 cm^{-1} indicated that all of the samples were quartz-rich. The absorption bands at 3696, 3622, 3450, 1033, 914, 790, 693, 538, and 468 cm^{-1} distinctly indicated that kaolinite was present in all of the samples. The observed absorption bands of kaolinite were in the agreement with findings of Yousefi et al. (2020). The clear signs of bands at 3696, 3622, 3450, 2369, 1633, 1033 and 790 cm^{-1} indicated that illite was also present in all of the core samples, and similar results were reported by previous researchers (Pineau et al. 2020). To differentiate kaolinite from illite, one should consider that the 1:1 layer clays (i.e., kaolinite) always show a narrow and weak absorption in

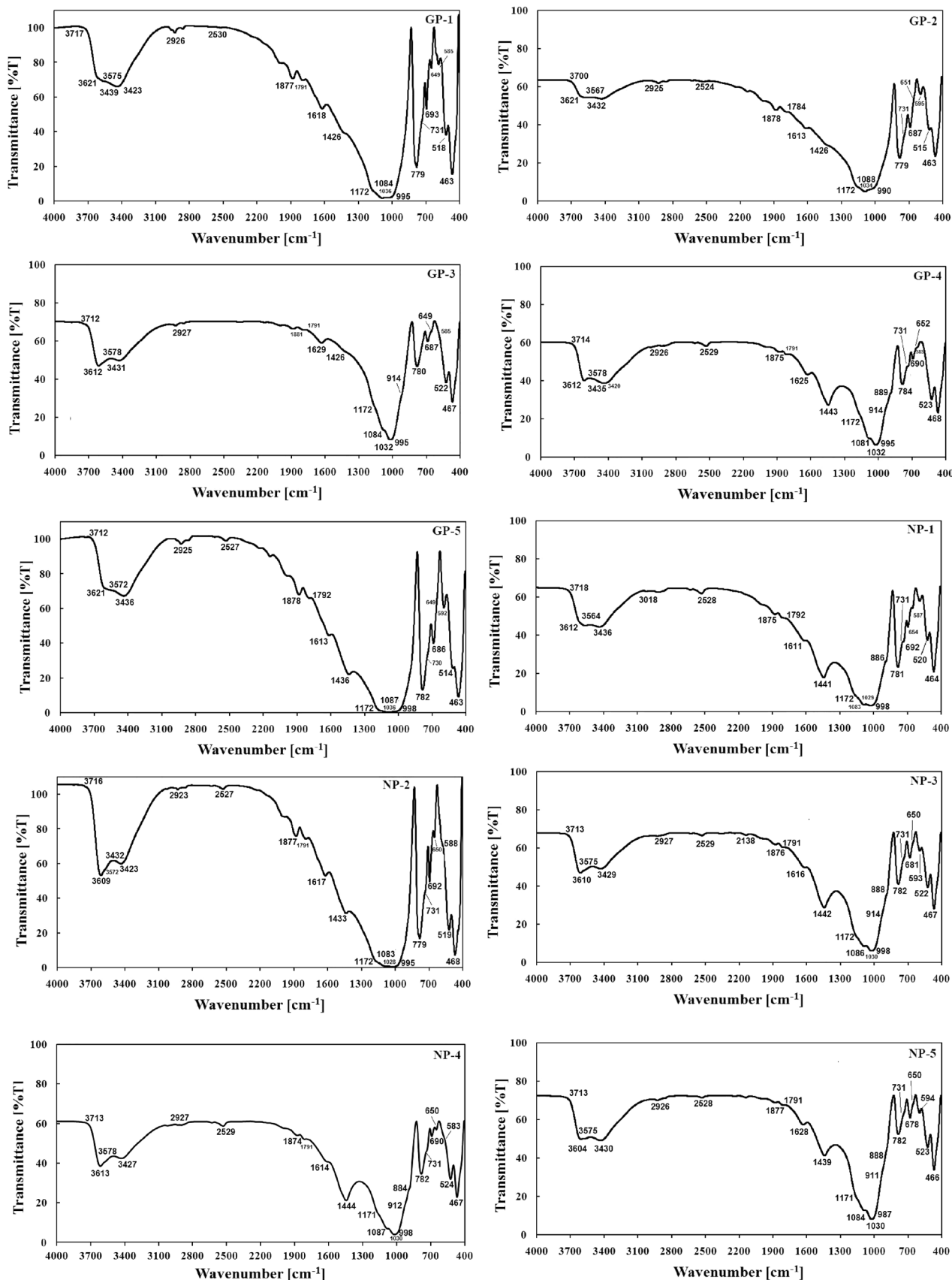


Fig. 5 FTIR spectra of core samples taken from the Shurijeh formation

Table 4 Important mineral IR bands with their possible assignments (Farmer 2000; Balan et al. 2001; Nayak & Singh 2007)

Band (cm ⁻¹)	Assignment
3703	Surface hydroxyls
3695	In-phase symmetric stretching vibration; internal surface OH groups
3669	Out-of-plane OH stretching vibrations
3653	Vibrations of two surface hydroxyls
3620	Inner OH groups, lying between the sheets of tetrahedral and octahedral units
3430	Adsorbed water vibrations (H–O–H)
1633	H–O–H stretching
1111	Stretch vibration modes of SO ₄ tetrahedra
1102	Stretch vibration modes of SO ₄ tetrahedra
1033	Si–O–Si, Si–O stretching
1094	Stretch vibration modes of SO ₄ tetrahedra
938	Deformation bands of kaolinite
914	Al ₂ OH bending bands of kaolinite AL–O–H vibrations
844	AlMgOH
790	Si–O stretching, Si–O–Al stretching, (Al, Mg)–O–H, Si–O–(Mg, Al) stretching
693	Si–O stretching, Si–O–Al stretching
538	Si–O bending, Si–O–Al stretching
468	Si–O bending, Si–O–Fe stretching

3600 cm⁻¹, while 2:1 layer clays (i.e., illite) display wide absorption in the 2600–3650 cm⁻¹ accompanied by a shoulder peak. The band at 914 cm⁻¹ was only observed in samples containing more than 6% illite (e.g., GP-3, GP-4, NP-3, NP-4, and NP-5). The absorption bands at 3560 cm⁻¹, 3542–3534 cm⁻¹, 1076 cm⁻¹, 995 cm⁻¹, and 463 cm⁻¹ were interpreted as being due to the presence of glauconite. Peaks near 3574 cm⁻¹, 3420 cm⁻¹, 1630 cm⁻¹, 1090 cm⁻¹, 995 cm⁻¹, 740–700 cm⁻¹, 661–650 cm⁻¹, and 522 cm⁻¹ were assigned to magnesium-rich chlorite. Characteristic features at 3621 cm⁻¹, 3420 cm⁻¹, 1039 cm⁻¹, 914 cm⁻¹, and 468 cm⁻¹ were considered for the smectite presence. Whereas 1111 cm⁻¹, 1102 cm⁻¹, 1094 cm⁻¹, 1015 cm⁻¹, 610 cm⁻¹, 659 cm⁻¹, and 591 cm⁻¹ were indicative of anhydrite, 3020 cm⁻¹, 2922 cm⁻¹, 2874 cm⁻¹, 2626 cm⁻¹, 1798 cm⁻¹, 1426 cm⁻¹, 876 cm⁻¹, and 730 cm⁻¹ showed the possibility of the carbonate presence. Core samples containing mixed-layer clay minerals showed overlapped absorptions of both clay types which were interlayered together. For instance, the overlap of illite absorption band at 3630 cm⁻¹ with smectite at 3635 and 3406 cm⁻¹ (due to the occurrence of absorption of interlayer water) were observed in the samples containing mixed-layer illite–smectite.

Peak assignments were mostly consistent with those in the previous literature (Repacholi 1994; Madejová & Komadel 2001; Madejová, 2003; Vaculíková & Plevová, 2005; Changwen et al. 2007; Nayak & Singh 2007; Ji et al. 2009; Liu et al. 2009; Papakosta et al. 2020; Pineau et al. 2020; Yousefi et al. 2020).

Discussion

From Fig. 5, it was obvious that the clay minerals were present in all samples; thus, it was decided to check the accuracy of FTIR prediction with XRD, and XRF methods to demonstrate the clay minerals existence in the samples.

It is clear from the results of the WDXRF test (Table 1) that the silicon was present in the major quantities in both wells, while the aluminum oxide was moderate and the other elements such as sulfur, calcium, potassium, sodium, magnesium, and iron were present in only minor amounts. Considering the mineralogy of the Shurijeh, the obtained results are meaningful.

The combined bulk powder X-ray diffractometry, X-ray fluorescence, and scanning electron microscopy (SEM) analyses of core samples showed that the main mineral constituents were quartz and plagioclase, with some quantities of other minerals such as the clay minerals, anhydrite, carbonates (calcite/dolomite), alkali feldspars, and hematite. The most important advantage of quantification using the XRF data is to allow for the quantitative calculations without the presence of any standard sample. The vast majority of clay minerals in the studied wells were illite, chlorite, and kaolinite. The most abundant clay mineral was illite in the both wells, but in few samples, there were signs of glauconite, smectite and mixed-layer clay minerals including I/S (illite–smectite) and chlorite–smectite. Among these rarely occurred clay minerals, glauconite was more common, while the smectite and

Table 5 Shurijeh formation FTIR bands with mineral assignments

Code	Mineral assignments (Band)
GP-1	Quartz (1877, 1172, 1084, 779, 693, 518, and 463 cm^{-1}), feldspar (1036, splitting bands in the region 800–400 cm^{-1} including 779, 693, 585, and 463 cm^{-1}), traces of carbonates (2926, 2530, 1791, 1426, and 731 cm^{-1}), traces of anhydrite (995 and 585 cm^{-1}), illite (3621, 3439, 1036, and 518 cm^{-1}), magnesium-rich chlorite (3575, 3423, 1618, 1084, 995, 693, 649, and 518 cm^{-1}), kaolinite (3717, 3621, 3439, 1036, 693, and 463 cm^{-1}), and glauconite (3575, 1084, 995, and 463 cm^{-1})
GP-2	Quartz (1878, 1172, 1088, 779, 687, 515, and 463 cm^{-1}), feldspar (1034, splitting bands in the region 800–400 cm^{-1} including 779, 687, 595, and 463 cm^{-1}), anhydrite (990 and 595 cm^{-1}), traces of carbonates (2926, 2524, 1784, 1426, and 731 cm^{-1}), illite (3621, 3432, 1034, and 515 cm^{-1}), magnesium-rich chlorite (3567, 3432, 1613, 1088, 990, 687, 651, and 515 cm^{-1}), kaolinite (3700, 3621, 3432, 1034, 687, and 463 cm^{-1}), and glauconite (3567, 1088, 990, and 463 cm^{-1})
GP-3	Quartz (1881, 1172, 1084, 780, 687, 522, and 467 cm^{-1}), feldspar (1032, splitting bands in the region 800–400 cm^{-1} including 780, 687, 585, and 467 cm^{-1}), traces of carbonates (2927, 1791, and 1426 cm^{-1}), traces of anhydrite (995 and 585 cm^{-1}), traces of hematite (649 and 522 cm^{-1}), illite (3612, 3431, 1032, 914, and 522 cm^{-1}), magnesium-rich chlorite (3578, 3431, 1629, 1084, 995, 687, 649, and 522 cm^{-1}), and kaolinite (3712, 3612, 3431, 1032, 687, and 467 cm^{-1})
GP-4	Quartz (1875, 1172, 1081, 784, 690, 523, and 468 cm^{-1}), feldspar (1032, splitting bands in the region 800–400 cm^{-1} including 784, 690, 585, and 468 cm^{-1}), carbonates (2926, 2529, 1791, 1443, 889, and 731 cm^{-1}), traces of hematite (652 and 523 cm^{-1}), illite (3612, 3435, 1032, 914, and 523 cm^{-1}), magnesium-rich chlorite (3578, 3435, 1625, 1081, 995, 690, 652, and 523 cm^{-1}), kaolinite (3714, 3612, 3435, 1032, 690, and 468 cm^{-1}), and smectite (3612, 3420, 1032, 914, and 468 cm^{-1})
GP-5	Quartz (1878, 1172, 1087, 782, 686, 514, and 463 cm^{-1}), feldspar (1036, splitting bands in the region 800–400 cm^{-1} including 782, 686, 592, and 463 cm^{-1}), anhydrite (998 and 592 cm^{-1}), traces of carbonates (2925, 2527, 1792, 1436, and 730 cm^{-1}), illite (3621, 3436, 1036, and 514 cm^{-1}), magnesium-rich chlorite (3572, 3436, 1613, 1087, 998, 686, 649, and 514 cm^{-1}), kaolinite (3712, 3621, 3436, 1036, 686, and 463 cm^{-1}), and glauconite (3572, 1087, 998, and 463 cm^{-1})
NP-1	Quartz (1875, 1172, 1083, 781, 692, 520, and 464 cm^{-1}), feldspar (1029, splitting bands in the region 800–400 cm^{-1} including 781, 692, 587, and 464 cm^{-1}), carbonates (3018, 2528, 1792, 1441, 886, and 731 cm^{-1}), traces of anhydrite (998 and 587 cm^{-1}), illite (3612, 3436, 1029, and 520 cm^{-1}), magnesium-rich chlorite (3564, 3436, 1611, 1083, 998, 692, 654, and 520 cm^{-1}), kaolinite (3718, 3436, 1029, 692, and 464 cm^{-1}), and glauconite (3564, 1083, 998, 464 cm^{-1})
NP-2	Quartz (1877, 1172, 1083, 779, 692, 519, and 468 cm^{-1}), feldspar (1028, splitting bands in the region 800–400 cm^{-1} including 779, 692, 588, and 468 cm^{-1}), traces of carbonates (2923, 2527, 1791, 1433, and 731 cm^{-1}), traces of anhydrite (995 and 588 cm^{-1}), traces of hematite (650 and 519 cm^{-1}), illite (3609, 3432, 1028, and 519 cm^{-1}), magnesium-rich chlorite (3572, 3423, 1617, 1083, 995, 692, 650, and 519 cm^{-1}), and kaolinite (3716, 3609, 3432, 1028, 692, and 468 cm^{-1}), and glauconite (3572, 1083, 995, and 468 cm^{-1})
NP-3	Quartz (1876, 1172, 1086, 782, 681, 522, and 467 cm^{-1}), feldspar (1030, splitting bands in the region 800–400 cm^{-1} including 782, 681, 593, and 467 cm^{-1}), carbonates (2927, 2529, 1791, 1442, 888, and 731 cm^{-1}), anhydrite (998 and 593 cm^{-1}), traces of hematite (650 and 522 cm^{-1}), illite (3610, 3429, 1030, 914, and 522 cm^{-1}), magnesium-rich chlorite (3575, 3429, 1616, 1086, 998, 681, 650, and 522 cm^{-1}), and kaolinite (3713, 3610, 3429, 1030, 681, and 467 cm^{-1})
NP-4	Quartz (1874, 1171, 1087, 782, 690, 524, and 467 cm^{-1}), feldspar (1030, splitting bands in the region 800–400 cm^{-1} including 782, 690, 583, and 467 cm^{-1}), carbonates (2927, 2529, 1791, 1444, 884, and 731 cm^{-1}), traces of anhydrite (998 and 583 cm^{-1}), traces of hematite (650 and 524 cm^{-1}), illite (3613, 3427, 1030, 912, and 524 cm^{-1}), magnesium-rich chlorite (3578, 3427, 1614, 1087, 998, 690, 650, and 524 cm^{-1}), and kaolinite (3713, 3613, 3427, 1030, 690, and 467 cm^{-1})
NP-5	Quartz (1877, 1171, 1084, 782, 678, 523, and 466 cm^{-1}), feldspar (1030, splitting bands in the region 800–400 cm^{-1} including 782, 678, 594, and 466 cm^{-1}), carbonates (2926, 2528, 1791, 1439, 888, and 731 cm^{-1}), anhydrite (987 and 594 cm^{-1}), traces of hematite (650 and 523 cm^{-1}), illite (3604, 3430, 1030, 911, and 523 cm^{-1}), magnesium-rich chlorite (3575, 3430, 1628, 1084, 987, 678, 650, and 523 cm^{-1}), and kaolinite (3713, 3604, 3430, 1030, 678, and 466 cm^{-1})

mixed-layer clays were only found in one or two samples of the non-producing well. The detailed quantitative XRD analysis yielded average clay mineral amounts which varied from 6.3 weight percent in the gas-producing well to the 18.8 weight percent in the non-producing well.

The wide variation in the percentage of clay minerals in the Shurijeh formation was due to the different depth of core samples. As a matter of fact, diagenetic changes occurred with an increase in the depth of burial which resulted in the generation of clay minerals. Apparently, the alteration of K-feldspar and plagioclase resulted in high amounts of illite. The existence of mixed-layer clay minerals proved that the smectite into illite transformation, a global phenomenon

(Blanc et al. 2021; Hucheng et al. 2021) was occurred in the Shurijeh formation with increasing depth too. Considering the impacts of clay mineralogy in a clastic reservoir (Ashraf et al. 2020, 2021), the illite, chlorite, and kaolinite could greatly affect on the reservoir parameters such as porosity and permeability.

The exact amount of each clay mineral in the both wells was determined by PXRD results which were combined by WDXRF data, and the XRD results played an important role on the evaluation of reservoir quality of the Shurijeh formation. Having known the volume of clay minerals, the reservoir parameters such as water saturation, porosity and permeability were estimated with more

accuracy (Jozanikohan 2017). It is known that an over/under-estimation of this parameter (V_{cl}) minerals can result in a wrong estimation of water saturations that are too low/high, therefore making the reservoir look productive or resulting in the bypassing of a productive zone. It can also effect on the calculation of effective porosities which are used to determine both the effective water saturations and the net pay (Causey 1991).

As a matter of fact, the FTIR pattern of a natural sample which includes a mixture of minerals is hard to interpret than for tests conducted on monomineralogical samples. Individual minerals in complex samples can be easily distinguished from each other, if enough attention is given. The O–H and Si–O groups of clay minerals make different absorption bands in the FTIR spectra over the range 4000–400 cm^{-1} , making it easy to differentiate each group of clay minerals. It is known that the most important region of the spectrum for the identification of aluminous minerals is the stretching vibrations of OH groups at 3800–3300 cm^{-1} (Pineau et al. 2020). However, this can be often hindered by absorbed water. The other main absorption region in transmittance spectra of clay minerals is 1200–400 cm^{-1} (Si–O stretching and bending absorptions, and OH bending region). The stretching modes of Al–O are found in the 1200–700 cm^{-1} range, while the bending modes dominate the 1500–600 cm^{-1} range (Madejová 2003). Any metal–O–H bending modes appear in the 600–950 cm^{-1} region (Farmer 2000). The absorption near 3620 cm^{-1} is typical for aluminum-rich clay minerals. The absorption bands for dioctahedral clay mineral are located in the 950–800 cm^{-1} , while the absorption are shifted to lower regions in the range of 700–600 cm^{-1} in trioctahedral clay minerals (Madejová 2003). A slight change in the peak position of each sample was observed due to the substitutions in crystal-line structure of minerals.

The recognition of hematite in some samples is significant, because hematite can cement the clay minerals together and make it difficult to be recognized with other analytical methods.

The result of infrared analysis evidently supported the mineral identification by PXRD method, and thus could be reliably used in fast clarifying the nature of the mineral constituents in formations with complex lithology. However, overlaps of some absorption, i.e., the splitting bands in OH region 4000–3000 cm^{-1} , due to the presence of different mineral species, might make it difficult to distinguish different minerals from each other at the first sight.

Since the first stage in the shale gas and shale oil exploration or in the mineralogical characterization of reservoirs needs to screen a lot of samples in an optimal manner in

terms of time and cost, the application of FTIR method as an easy and fast data providing method with less costs can be considered.

Conclusions

In particular, transmission Fourier transform infrared spectroscopy (FTIR) showed merits as an inexpensive, easy, and fast method in differentiating several types of clay minerals in the formations with complex lithology such as Shurijeh formation. The FTIR is also able to provide fundamental information on the clay minerals. All in one, the ease of use and the speed of the method have made the FTIR a suitable initial analysis for the purpose of clay minerals studies in reservoir characterization stages. The results obtained from this research can be a benefit to the geoscientists in upstream petroleum industry to screen the samples very fast before conducting more sophisticated and time-consuming analysis methods with the purpose of chemical and mineralogical characterizations, because the FTIR is able to do the both tasks, with more convenience and less costs. This method can be applied on the clastic reservoirs or on the shale oil and shale gas targets to be quickly assessed in terms of their potential. A series of Shurijeh core samples have been used to illustrate the usefulness of the technique in this study.

Acknowledgements Acknowledgements are due to the X-Ray laboratory, School of Mining, College of Engineering, University of Tehran, for kind participation and collaborations made throughout the present study.

Authors' contributions The first author has contributed to conducting the research as well as the interpretation of the results. The second author has taken the lead in writing the manuscript.

Funding This research received no specific grant from any funding agency in the public, commercial, or not-for-profit sectors.

Data availability The research data associated with this paper is available; it can be accessed, if anyone just emails the corresponding author.

Declarations

Conflict of interest Two authors of the paper declare that they have no conflict of interest.

Consent for publication The both authors give our consent for the publication of identifiable details, which can include figures, tables, case history, and details within the text (“Material”) to be published in the Journal of Petroleum Exploration and Production Technology.

Ethics approval This material is the authors' own original work, which has not been previously published elsewhere. The paper is not currently being considered for publication elsewhere. The paper reflects the authors' own research and analysis in a truthful and complete manner. All procedures performed in studies involving performing the tests were in accordance with the ethical standards of the world.

Open Access This article is licensed under a Creative Commons Attribution 4.0 International License, which permits use, sharing, adaptation, distribution and reproduction in any medium or format, as long as you give appropriate credit to the original author(s) and the source, provide a link to the Creative Commons licence, and indicate if changes were made. The images or other third party material in this article are included in the article's Creative Commons licence, unless indicated otherwise in a credit line to the material. If material is not included in the article's Creative Commons licence and your intended use is not permitted by statutory regulation or exceeds the permitted use, you will need to obtain permission directly from the copyright holder. To view a copy of this licence, visit <http://creativecommons.org/licenses/by/4.0/>.

References

- Abd Elmola A, Asaad A, Patrier P, Beaufort D, Ballini M, Descostes M (2020) Clay mineral signatures of fault-related fluid flows in a sandstone reservoir: A case study from the Teloua Formation, Tim Mersoï Basin Niger. *J African Earth Sci* 168:103840
- Abudeif AM, Attia MM, Radwan AE (2016a) Petrophysical and petrographic evaluation of Sidri member of Belayim Formation, Badri field, Gulf of Suez Egypt. *J African Earth Sci* 115:108–120
- Abudeif AM, Attia MM, Radwan AE (2016b) New simulation technique to estimate the hydrocarbon type for the two untested members of Belayim Formation in the absence of pressure data, Badri Field, Gulf of Suez Egypt. *Arabian J Geosci* 9(3):218
- Abudeif AM, Attia MM, Al-Khashab HM, Radwan AE (2018) Hydrocarbon type detection using the synthetic logs: a case study, Baba member, Gulf of Suez Egypt. *J African Earth Sci* 144:176–182
- Adamu MB (2010) Fourier transform infrared spectroscopic determination of shale minerals in reservoir rocks. *Nigerian J Basic Appl Sci* 18(1):6–18
- Ali M, Ma H, Pan H, Ashraf U, Jiang R (2020) Building a rock physics model for the formation evaluation of the lower Goru sand reservoir of the Southern Indus Basin in Pakistan. *J Petrol Sci Eng* 194:107461
- Ashraf U, Zhu P, Yasin Q, Anees A, Imraz M, Mangi HN, Shakeel S (2019) Classification of reservoir facies using well log and 3D seismic attributes for prospect evaluation and field development: a case study of Sawan gas field, Pakistan. *J Petrol Sci Eng* 175:338–351
- Ashraf U, Zhang H, Anees A, Ali M, Zhang X, Shakeel Abbasi S, Nasir Mangi H (2020) Controls on reservoir heterogeneity of a shallow-marine reservoir in Sawan gas field, SE Pakistan: implications for reservoir quality prediction using acoustic impedance inversion. *Water* 12(11):2972
- Ashraf U, Zhang H, Anees A, Mangi HN, Ali M, Zhang X, Tan S (2021) A core logging, machine learning and geostatistical modeling interactive approach for subsurface imaging of lenticular geobodies in a clastic depositional system SE Pakistan. *Nat Resour Res* 30(3):2807–2830
- Attia MM, Abudeif AM, Radwan AE (2015) Petrophysical analysis and hydrocarbon potentialities of the untested Middle Miocene Sidri and Baba sandstone of Belayim Formation, Badri field, Gulf of Suez. *Egypt J African Earth Sci* 109:120–130
- Balan E, Saitta AM, Mauri F, Calas G (2001) First-principles modeling of the infrared spectrum of kaolinite. In: *American mineralogist*. pp 1321–1330
- Blanc P, Gherardi F, Vieillard P, Marty NCM, Gailhanou H, Gaboreau S et al (2021) Thermodynamics for clay minerals: Calculation tools and application to the case of illite/smectite interstratified minerals. *Appl Geochem* 130:104986
- Bodine MW, Fernald TH (1973) EDTA dissolution of gypsum, anhydrite, and Ca-Mg carbonates. *J Sediment Res* 43:4 (1152,1156)
- Causey GL (1991) Computer determination and comparison of volume of clay derived from petrophysical and laboratory analysis (Doctoral dissertation, Texas Tech University)
- Changwen D, Linker R, Shaviv A (2007) Characterization of soils using photoacoustic mid-infrared spectroscopy. In: *applied spectroscopy*. pp 1063–1067
- Chen H, Li Q, Wang M, Ji D, Tan W (2020) XPS and two-dimensional FTIR correlation analysis on the binding characteristics of humic acid onto kaolinite surface. *Sci Total Environ* 724:138154
- Djomgoue P, Njopwouo D (2013) FT-IR spectroscopy applied for surface clays characterization. *J Surface Eng Mater Adv Technol* 3(4):275–282
- Du C, Zhou G, Deng J, Zhou J (2010). Characterization of soil clay minerals using mid-infrared spectroscopy. In: *molecular environmental soil science at the interfaces in the earth's critical zone* (pp 265–268). Springer, Berlin, Heidelberg
- El-Shater A, Mansour AM, Osman MR, Abd El Ghany AA, Abd El-Samee A (2021) Evolution and significance of clay minerals in the Esna Shale formation at Dababiya area, Luxor Egypt. *Egypt J Pet* 30(2):9–16
- Farmer VC (2000) Transverse and longitudinal crystal modes associated with OH stretching vibrations in single crystals of kaolinite and dickite. In: *spectrochimica acta part A: molecular and biomolecular spectroscopy*. pp 927–930
- Hasan MN, Yeasmin R, Rahman M, Potter-McIntyre S (2020) Diagenetic clay minerals and their controls on reservoir properties of the Shahbazpur gas field (Bengal Basin, Bangladesh). *Geosciences* 10(7):250
- Hong D, Cao J, Wu T, Dang S, Hu W, Yao S (2020) Authigenic clay minerals and calcite dissolution influence reservoir quality in tight sandstones: insights from the central Junggar Basin. *NW China Energy Geosci* 1(1–2):8–19
- Hucheng D, Meiyang F, Wen Z, Liying Z, Xinhui X, Yilin L et al (2021) The pores evolution of lacustrine shale induced by smectite-to-illite conversion and hydrocarbon generation: upper Triassic Yanchang Formation, Ordos Basin, China. *J Petrol Sci Eng* 202:108460
- Jackson ML, Barak P (2005) *Soil chemical analysis: advanced course*. UW-Madison Libraries Parallel Press
- Ji J, Ge Y, Balsam W, Damuth JE, Chen J (2009) Rapid identification of dolomite using a Fourier transform infrared spectrophotometer (FTIR): a fast method for identifying Heinrich events in IODP Site U1308. *Mar Geol* 258(1–4):60–68
- Jiu B, Huang W, Li Y, He M (2021) Influence of clay minerals and cementation on pore throat of tight sandstone gas reservoir in the eastern Ordos Basin, China. *J Nat Gas Sci Eng* 87:103762
- Jozanikohan G (2017) On the development of a non-linear calibration relationship for the purpose of clay content estimation from the natural gamma ray log. *Int J Geo-Eng* 8(1):21
- Jozanikohan G, Norouzi GH, Sahabi F, Memarian H, Moshiri B (2015) The application of multilayer perceptron neural network in volume of clay estimation: case study of Shurijeh gas reservoir, Northeastern Iran. *J Nat Gas Sci Eng* 22(1):119–131
- Jozanikohan G, Sahabi F, Norouzi GH, Memarian H, Moshiri B (2016) Quantitative analysis of the clay minerals in the Shurijeh reservoir Formation using combined X-ray analytical techniques. *Russian Geol Geophys* 57(7):1048–1063
- Kasprzhitskii A, Lazorenko G, Khater A, Yavna V (2018) Mid-infrared spectroscopic assessment of plasticity characteristics of clay soils. *Minerals* 8(5):184
- Kuligiewicz A, Derkowski A (2017) Tightly bound water in smectites. *W Druku, Am Mineralogist*. <https://doi.org/10.2138/am-2017-5918>
- Kumar A, Lingfa P (2020) Sodium bentonite and kaolin clays: comparative study on their FT-IR, XRF, and XRD. *Mater Today Proc* 22:737–742

- Li R, Parnell J (2003) In situ microanalysis of petroleum fluid inclusions by Time of Flight-Secondary Ion Mass Spectrometry as an indicator of evolving oil chemistry: a pilot study in the Bohai Basin, China. *J Geochem Explor* 78:377–384
- Li, Y. (2009) Analysis of Acidity in Oil-Based Matrices by Infrared Spectroscopy. Master thesis, department of Food Science & Agricultural Chemistry, Macdonald Campus, McGill University Montreal, Quebec, Canada
- Lin R, Ritz GP (1993) Studying individual macerals using infrared microspectrometry, and implications on oil versus gas/condensate proneness and “low-rank” generation. *Org Geochem* 20(6):695–706
- Liu Y, Wang A, Freeman JJ (2009) Raman, MIR, and NIR spectroscopic study of calcium sulfates: gypsum, bassanite, and anhydrite. In: lunar and planetary science conference. pp 2128–2129
- Ma F, Du C, Zhang Y, Xu X, Zhou J (2021) LIBS and FTIR-ATR spectroscopy studies of mineral–organic associations in saline soil. *Land Degrad Dev* 32(4):1786–1795
- Madejová J, Komadel P (2001) Baseline studies of the clay minerals society source clays: infrared methods. In: clays and clay minerals. pp 410–432
- Madejová J, Bujdak J, Janek M, Komadel P (1998) Comparative FT-IR study of structural modifications during acid treatment of dioctahedral smectites and hectorite. In: *spectrochimica acta part a: molecular and biomolecular spectroscopy*. pp 1397
- Madejová J (2003) FTIR techniques in clay mineral studies. In: *Vibrational spectroscopy*. pp 1–10
- Matteson A, Herron MM (1993) Quantitative mineral analysis by Fourier transform infrared spectroscopy. In: SCA conference (No. 9308)
- Meunier A (2005) *Clays*. Springer Science & Business Media, Berlin
- Moore DM, Reynolds RC (1989) *X-ray Diffraction and the Identification and Analysis of Clay Minerals*. Oxford University Press, Oxford
- Nayak PS, Singh BK (2007) Instrumental characterization of clay by XRF, XRD and FTIR. *Bull Mater Sci* 30:235–238
- Paktunc AD (2001) MODAN—a computer program for estimating mineral quantities based on bulk composition: windows version. *Comput Geosci-UK* 27(7):883–886
- Pálková H, Kureková V, Madejová J, Netrová Z, Uhlík P, Varga P et al (2020) Determination of water content in raw perlites: Combination of NIR spectroscopy and thermoanalytical methods. *Spectrochimica Acta Part a: Mol Biomol Spectroscopy* 240:118517
- Papakosta V, Lopez-Costas O, Isaksson S (2020) Multi-method (FTIR, XRD, PXRF) analysis of Ertebølle pottery ceramics from Scania, southern Sweden. *Archaeometry* 62(4):677–693
- Pineau M, Baron F, Mathian M, Le Deit L, Rondeau B, Allard T, et al (2020). Estimating kaolinite crystallinity using near-infrared spectroscopy. In: 51st Lunar and planetary science conference
- Prandel LV, Saab SC, Brinatti AM, Giarola NFB, Leite WC, Cassaro FAM (2014) Mineralogical analysis of clays in hardsetting soil horizons, by X-ray fluorescence and X-ray diffraction using Rietveld method. *Radiat Phys Chem* 95:65–68
- Primpke S, Fischer M, Lorenz C, Gerdtz G, Scholz-Böttcher BM (2020) Comparison of pyrolysis gas chromatography/mass spectrometry and hyperspectral FTIR imaging spectroscopy for the analysis of microplastics. *Anal Bioanal Chem* 412(30):8283–8298
- Radwan AE (2021a) Modeling the depositional environment of the sandstone reservoir in the Middle Miocene Sidri Member, Badri Field, Gulf of Suez Basin, Egypt: integration of gamma-ray log patterns and petrographic characteristics of lithology. *Nat Resour Res* 30(1):431–449
- Radwan AE (2021b) Integrated reservoir, geology, and production data for reservoir damage analysis: a case study of the Miocene sandstone reservoir, Gulf of Suez Egypt. *Interpretation* 9(4):SH27–SH37
- Radwan AE, Abudeif AM, Attia MM, Mahmoud MA (2019) Development of formation damage diagnosis workflow, application on Hammam Faraun reservoir: a case study, Gulf of Suez Egypt. *J African Earth Sci* 153:42–53
- Radwan AE, Abudeif AM, Attia MM (2020) Investigative petrophysical fingerprint technique using conventional and synthetic logs in siliciclastic reservoirs: a case study, Gulf of Suez basin Egypt. *J African Earth Sci* 167:103868
- Radwan AE, Nabawy BS, Kassem AA, Hussein WS (2021b) Implementation of rock typing on waterflooding process during secondary recovery in oil reservoirs: a case study, El Morgan Oil Field, Gulf of Suez. *Egypt Nat Resour Res* 30(2):1667–1696
- Radwan AE, Rohais S, Chiarella D (2021a). Combined stratigraphic-structural play characterization in hydrocarbon exploration: a case study of Middle Miocene sandstones, Gulf of Suez basin, Egypt. *J Asian Earth Sci*, 104686
- Radwan AE, Wood DA, Abudeif AM, Attia MM, Mahmoud M, Kassem AA, Kania M (2021c). Reservoir formation damage; reasons and mitigation: a case study of the Cambrian–Ordovician Nubian ‘C’ Sandstone Gas and Oil Reservoir from the Gulf of Suez Rift Basin. *Arabian J Sci Eng*, 1–18
- Radwan AE (2020). Effect of clay minerals in oil and gas formation damage problems and production decline: a case study, Gulf of Suez, Egypt. *AAPG/datapages*
- Repacholi MH (1994) *Clay mineralogy: spectroscopic and chemical determinative methods*. Springer Science & Business Media, Berlin
- Scholze B, Meier D (2001) Characterization of the water-insoluble fraction from pyrolysis oil (pyrolytic lignin). Part I. PY–GC/MS, FTIR, and functional groups. *J Analytic Appl Pyroly* 60(1):41–54
- Shen DK, Gu S, Bridgwater AV (2010) Study on the pyrolytic behaviour of xylan-based hemicellulose using TG–FTIR and Py–GC–FTIR. *J Anal Appl Pyroly* 87(2):199–206
- Stanienda K (2016) Mineral phases in carbonate rocks of the Górażdże beds from the area of Opole Silesia. *Gospodarka Surowcami Mineralnymi* 32(3):67–92
- Tyagi B, Chudasama CD, Jasra RV (2006) Determination of structural modification in acid activated montmorillonite clay by FT-IR spectroscopy. *Spectrochimica Acta Part a: Mol Biomol Spectroscopy*. 46(2):273–278
- Uusitalo S, Soudunsaari T, Sumen J, Haavisto O, Kaartinen J, Huuskonen J et al (2020) Online analysis of minerals from sulfide ore using near-infrared Raman spectroscopy. *J Raman Spectrosc* 51(6):978–988
- Vaculíková L, Plevová E (2005) Identification of clay minerals and micas in sedimentary rocks. *Acta Geodynamica Et Geomaterialia* 2(2):67–175
- Wang R, Shi W, Xie X, Zhang W, Qin S, Liu K et al (2020) Clay mineral content, type, and their effects on pore throat structure and reservoir properties: Insight from the Permian tight sandstones in the Hangjinqi area, north Ordos Basin China. *Marine Petroleum Geol* 115:104281
- Worasith N, Goodman BA, Neampan J, Jeyachoke N, Thiravetyan P (2011) Characterization of modified kaolin from the Ranong deposit Thailand by XRD, XRF, SEM FTIR and EPR Techniques. *Clay Miner* 46(4):539–559
- Wright MC, Court RW, Kafantaris FCA, Spathopoulos F, Sephton MA (2015) A new rapid method for shale oil and shale gas assessment. *Fuel* 153:231–239
- Yan B, Liu S, Chastain ML, Yang S, Chen J (2021) A new FTIR method for estimating the firing temperature of ceramic bronze-casting moulds from early China. *Sci Rep* 11(1):1–10
- Yousefi B, Castanedo CI, Maldague XP, Beaudoin G (2020) Assessing the reliability of an automated system for mineral identification using LWIR hyperspectral infrared imagery. *Minerals Eng* 155:106409

- Zhang X, Zhang H, Chang F, Ashraf U, Peng W, Wu H, Duan L (2020) Application of corrected methods for high-resolution XRF core scanning elements in lake sediments. *Appl Sci* 10(22):8012
- Zhang X, Zhang H, Chang F, Ashraf U, Wu H, Peng W, Duan L (2021) Sedimentary grain-size record of Holocene runoff fluctuations in the Lake Lugu watershed. *SE Tibetan Plateau Holocene* 31(3):346–355

Publisher's Note Springer Nature remains neutral with regard to jurisdictional claims in published maps and institutional affiliations.